ADVANCING EARTH AND SPACE SCIENCE

Geophysical Research Letters

RESEARCH LETTER
10.1029/2020GL090142

Present-Day Deformation Mechanism of the Northeastern Mina Deflection Revealed by the 2020 M_w 6.5 Monte Cristo Range Earthquake

Ao Zheng[1,2], Xiaofei Chen[2], and Wenbin Xu[3,4]

[1]School of Earth and Space Sciences, University of Science and Technology of China, Hefei, China, [2]Department of Earth and Space Sciences, Southern University of Science and Technology, Shenzhen, China, [3]School of Geosciences and Info-Physics, Central South University, Changsha, China, [4]Key Laboratory of Metallogenic Prediction of Nonferrous Metals and Geological Environment Monitoring (Central South University), Ministry of Education, Changsha, China

Key Points:
- Source rupture process of the 2020 Monte Cristo Range earthquake is derived using joint inversion of geodetic and seismic data
- Two fault segments with varied orientations ruptured, producing oblique and sinistral slip on the western and eastern segments, respectively
- Accommodation of slip transfer in the northeastern Mina deflection tends to transform from wrench- to extension-dominated transtension

Supporting Information:
- Supporting Information S1

Correspondence to:
W. Xu,
wenbin.xu@csu.edu.cn

Citation:
Zheng, A., Chen, X., & Xu, W. (2020). Present-day deformation mechanism of the northeastern Mina deflection revealed by the 2020 M_w 6.5 Monte Cristo Range earthquake. *Geophysical Research Letters*, *47*, e2020GL090142. https://doi.org/10.1029/2020GL090142

Received 31 JUL 2020
Accepted 4 NOV 2020
Accepted article online 16 NOV 2020

Abstract The 15 May 2020 Monte Cristo Range M_w 6.5 earthquake occurred in the northeast of the Mina deflection, which accommodates approximately a quarter of the relatively dextral motion between the Pacific and North American plates. The Monte Cristo Range event provides an opportunity to study the present-day regional deformation mechanism and active tectonics. In this study, we investigate the source rupture process of the event using joint inversion of interferometric synthetic aperture radar and broadband seismic data. We find that the rupture propagates almost simultaneously on two main segments. The fault motion changes from the predominantly sinistral slip near the epicenter on the eastern segment to the oblique slip on the western segment, with a maximum coseismic slip of 0.8 m. Our results suggest that the accommodation of slip transfer localized in the northeastern Mina deflection tends to transform from the wrench- to extension-dominated transtension.

Plain Language Summary The relative motion between the Pacific and North American plates is largely focused on the dextral San Andreas fault system. A complex array of strike-slip and normal faults, known as the Walker Lane and the Eastern California shear zone, accommodates about a quarter of this plate motion. The 2020 Monte Cristo Range earthquake struck the Mina deflection, a right stepover between two parallel but noncoplanar faults. The Mina deflection is considered to transfer slip from the southern to central Walker Lane. Because of the obliquity between the plate motion and the fault orientation, the deformation across the Mina deflection is generally interpreted as wrench-dominated transtension, commonly characterized by strike slip and block rotation. We reconstruct the spatial and temporal process of the source rupture by integrated geodetic and seismological data analysis and find that the accommodation of slip transfer in the northeast of the Mina deflection has a tendency to evolve into the extension-dominated transtension, thereby harboring normal faulting. We suggest that this behavior is because the extensional pure shear accumulates more rapidly compared with the wrench simple shear.

1. Introduction

Geologic and geodetic studies indicate that the San Andreas fault system accommodates 75–80% of the relatively dextral motion between the Pacific and North American plates, with the Walker Lane and Eastern California shear zone accommodating the remaining 20–25% (Bennett et al., 2003; Dixon et al., 1995, 2000; Dokka & Travis, 1990). Subparallel to the Pacific-North American plate motion, the NW-trending dextral faults that define the Walker Lane are discontinuous and interrupted by zones of ENE-trending sinistral faults (Wesnousky, 2005b). This diffuse region may coalesce into a major transform boundary in the future and replace the San Andreas fault to assume the tectonic motion (Faulds et al., 2005). The Mina deflection is an ENE-trending stepover comprising dextral, sinistral, and normal faults, connecting the central and southern Walker Lane (Lee et al., 2009; Nagorsen-Rinke et al., 2013; Tincher et al., 2009; Wesnousky, 2005a).

The accommodation of slip transfer across the Mina deflection has been interpreted in several ways. Wesnousky (2005a) and Nagorsen-Rinke et al. (2013) suggested that the dextral slip transferred into the Mina deflection produced a clockwise vertical-axis rotation of the crustal block bounded by the ENE-trending sinistral faults. Conversely, Oldow (1992) and Oldow et al. (1994) proposed a

displacement-transfer model for the Mina deflection, whereby extensions across normal faults accommodate the dextral slips transferred between the southern and central Walker Lane. Subsequently, Oldow (2003) explained the deformation mechanism across the Mina deflection region using a transtensional model involving components of the wrench simple shear and extensional pure shear. The angular relationship between the incremental extensional axes and the dextral boundary faults determines whether the transtension is extension- or wrench-dominated. However, because the historical seismicity is rare for this area (Rogers et al., 1991) and previous studies primarily involved geological observations and data-based inversions, studying the source rupture process of an earthquake in the region is important to elucidate the regional deformation mechanism.

On 15 May 2020, a moderate M_w 6.5 earthquake, representing the highest magnitude incident in Nevada since the 1954 M_s 7.2 Fairview Peak and M_s 6.7 Dixie Valley earthquakes (Hodgkinson et al., 1996), struck the west of the Monte Cristo Range. The epicenter of the Monte Cristo Range earthquake is in the northeastern edge of the Mina deflection. The surface fractures discovered for this earthquake were not coherent enough to delineate the fault trace (Nevada Bureau of Mines and Geology, last accessed 24 July 2020, at http://www.nbmg.unr.edu/Geohazards/Earthquakes/MonteCristoRangeEQ.html), so the subsurface fault geometry was obscured. The slip distribution and rupture kinematics associated with the event were also hidden. This earthquake, however, occurred in a desert area that is suitable for the satellite interferometric synthetic aperture radar (InSAR) (Massonnet et al., 1993), and the coseismic offsets were recorded at global positioning system stations operated by the Nevada Geodetic Laboratory. Geodetic records of ground deformation can contribute in constraining source parameters for the seismogenic structure, whereas the seismic data can clarify the rupture process (Kikuchi & Kanamori, 1982).

Therefore, in this study, we utilize a seismo-geodetic inversion method integrating the InSAR and seismological waveform data to reproduce the spatiotemporal rupture process of the Monte Cristo Range earthquake. We also examine the source complexity including whether the earthquake involved the rupture of conjugate faults. This study provides insights into the deformation mechanism in the Mina deflection stepover.

2. Geodetic and Seismic Data Processing

2.1. Geodetic Data Processing

One Sentinel-1 interferogram acquired in the Ascending Track 64 and two in the Descending Tracks 71 and 144 were used to retrieve the coseismic line-of-sight (LOS) displacements covering the epicentral area (supporting information Table S1). By following the standard two-pass InSAR data processing method (Xu et al., 2016), we processed the interferograms using the GAMMA software. The 30 m Shuttle Radar Topography Mission digital elevation model was utilized to simulate and eliminate topographic signals (Farr et al., 2007). The interferograms were then filtered by an improved Goldstein filter (Li et al., 2008) and unwrapped using the minimum cost flow method (Chen & Zebker, 2001). Finally, the unwrapped interferograms were geocoded into the World Geodetic System 84 coordinate system. We checked the phase unwrapping results, masking areas with low coherence involving undetected unwrapping errors.

The measured LOS displacement d_{los} represents the projection of the surface displacement field (three orthogonal components: north, U_n; east, U_e; and up, U_u), and the look angles are computed pixelwise. Because the satellite heading vectors and incidence angles of the descending track data are close, obtaining an accurate solution for three displacement fields using the ascending and descending tracks data is difficult. Therefore, reasonable assumptions were made to obtain the horizontal and vertical displacements. Given that the source fault is oriented nearly east-west and the InSAR is least sensitive to north-south motion owing to its nearly polar orbits, the contribution of the north-south displacement component to the observed ground deformation is considered negligible. Therefore, we retrieved the east-west horizontal and vertical displacement fields by ignoring the north-south displacement component as following:

$$\begin{bmatrix} d_{los}^{T64} \\ d_{los}^{T71} \\ d_{los}^{T144} \end{bmatrix} = \begin{bmatrix} -\cos\varphi_{T64}\cdot\sin\theta_{T64} & \cos\theta_{T64} \\ -\cos\varphi_{T71}\cdot\sin\theta_{T71} & \cos\theta_{T71} \\ -\cos\varphi_{T144}\cdot\sin\theta_{T144} & \cos\theta_{T144} \end{bmatrix} \cdot \begin{bmatrix} U_e \\ U_u \end{bmatrix}, \tag{1}$$

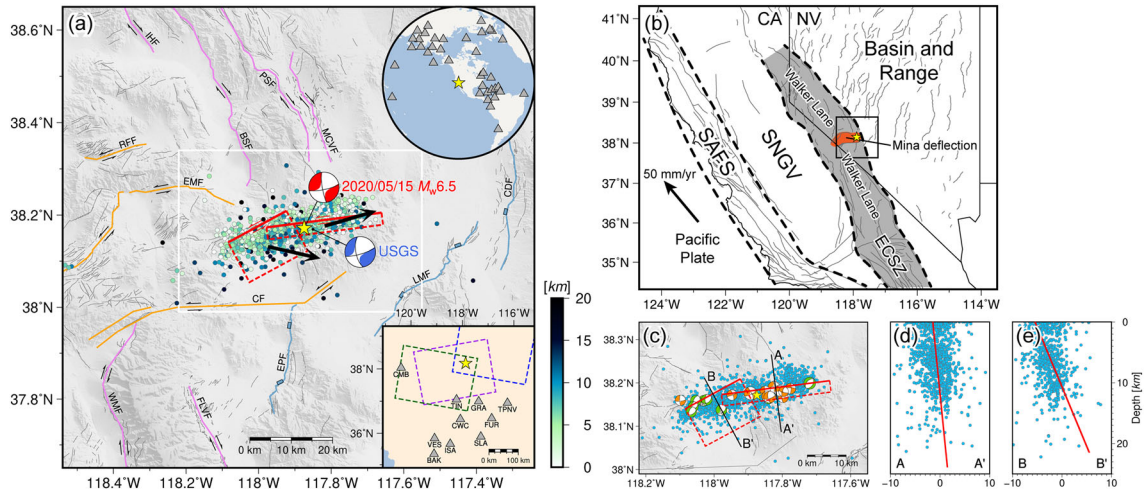

Figure 1. (a) Map showing the study area for the 2020 M_w 6.5 Monte Cristo Range earthquake. The beach ball in red shows the focal mechanism of the mainshock derived from the joint inversion. The *W*-phase moment tensor of the USGS-NEIC is depicted in blue. Red frames are the ground projections of the two-segment fault model, with the red solid lines indicating the top traces. Black arrows indicate the average rakes of corresponding fault segments. The yellow star is the rupture starting point (epicenter). Major dextral, sinistral, and normal faults (Petersen et al., 2014) are shown by lines of different colors. The rectangle with solid lines encloses the hanging wall of the normal faults, whereas the paired arrows indicate the relative motion across the strike-slip faults. Minor Quaternary faults (Quaternary fault and fold database for the United States, last accessed 15 July 2020 at https://www.usgs.gov/natural-hazards/earthquake-hazards/faults) are shown in gray lines. The white frame represents the area in (c). The fault abbreviations are IHF = Indian Head fault; BSF = Benton Springs fault; PSF = Petrified Springs fault; MCVF = Monte Cristo Valley fault; RFF = Rattlesnake Flat fault; EMF = Excelsior Mountains fault; CF = Coaldale fault; WMF = White Mountains fault; FLVF = Fish Lake Valley fault; EPF = Emigrant Peak fault; LMF = Lone Mountain fault; CDF = Crescent Dunes fault. The aftershocks that followed 5 days after the mainshock are plotted in circles with the colors corresponding to the focal depths. The gray triangles in both insets indicate the teleseismic and regional seismic stations. The colored dashed frames in the lower right inset represent the coverage of Sentinel-1 interferograms. (b) Map showing the location of the study area in relation to other elements of the Pacific/North American plate boundary zone. Pacific-North American relative plate motion vector is 50 mm/year at 323° (DeMets & Dixon, 1999). The Walker Lane and the Eastern California shear zone (ECSZ) are in dark gray; the Mina deflection is in orange. Other element abbreviations are SAFS = San Andreas fault system; SNGV = Sierra Nevada/Great Valley; CA = California; NV = Nevada. The black frame indicates the area in (a). (c) The aftershocks are plotted using blue circles, with the focal mechanisms of $M \geq 4$ aftershocks dominated by strike-slip and normal faulting shown separately in the orange and green beach balls. The red frames depict the ground projection of the two-segment fault model. (d and e) The cross-sections A-A′ and B-B′ perpendicular to the two fault segments, with the red line as the projection of the corresponding segment.

where d^i_{los} ($i = T64, T71, T144$) represents the LOS displacements acquired in Tracks 64, 71, and 144. φ_i and θ_i are the satellite heading vector (positive clockwise from the north) and the radar incidence angle, respectively.

2.2. Seismic Data Processing

We selected 38 teleseismic *P* waves at epicentral distances ranging between 30° and 90° (Figure 1a) from the database of the Data Management Center of the Incorporated Research Institutions for Seismology (IRIS DMC). The teleseismic stations in the southwestern azimuth were excluded because of the low signal-to-noise ratio of the associated data. The instrument response was removed from the initial records to produce displacement waveforms (Wald et al., 1996) and then band-pass filtered between 0.01 and 0.5 Hz. To improve the azimuthal coverage and expand the data types, three-component broadband seismograms of 10 regional stations located less than 300 km from the epicenter were also employed in the joint inversion. The corresponding waveforms were downloaded from the IRIS DMC database, with removal of the instrument response and band-pass filtering between 0.01 and 0.1 Hz.

3. Joint Inversion Strategy

The focal mechanism determined by the United States Geological Survey-National Earthquake Information Center (USGS-NEIC) for the mainshock indicates that the slip probably occurred on an EW-striking sinistral or a NS-striking dextral fault. The *W*-phase moment tensor shows a nondouble-couple component of ~32%, implying a complex source mechanism. From the east-west and vertical displacement fields (Figure 2), an area of large negative displacement representing subsidence is prominent west of the epicenter, which is consistent with the normal-faulting focal mechanisms of aftershocks (Figure 1c). This deformation

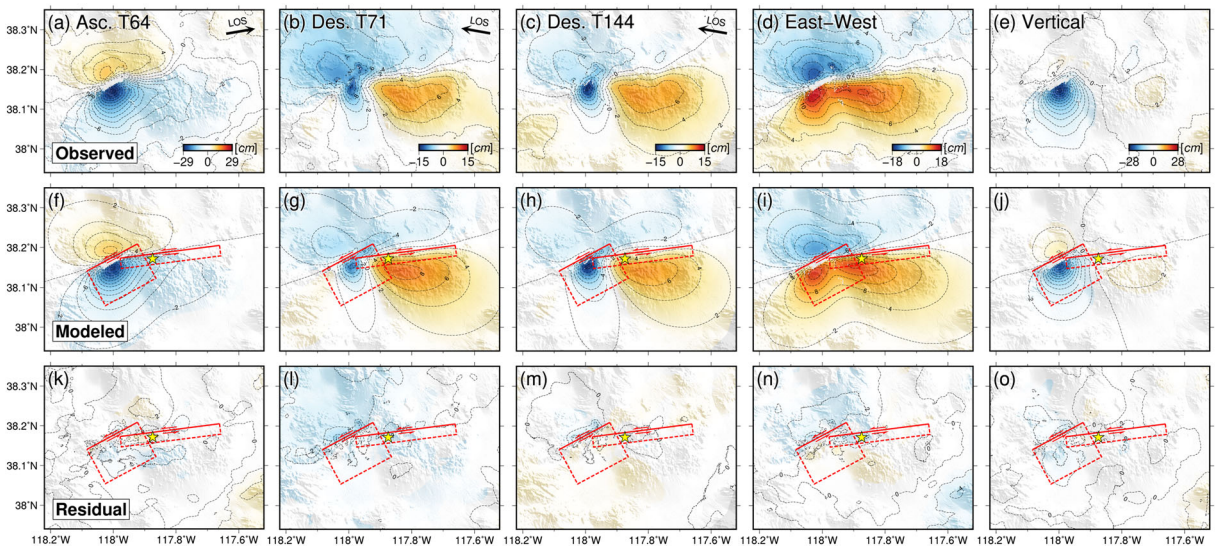

Figure 2. Coseismic InSAR LOS and two-dimensional surface displacement fields derived from Sentinel-1 interferograms for (a–e) the observed displacement fields, (f–j) the modeled displacement fields using our preferred two-segment fault model, and (k–o) the residuals. In the east-west horizontal displacement field (d), the warm color shows the eastward displacement, and the cold color displays the westward displacement. In the vertical displacement field (e), the cold color represents the subsidence-related displacement. The red dashed frames in (f)–(o) are the surface projections of the two-segment fault model, with the yellow star representing the epicenter.

pattern orients in an ENE direction suggesting the strike of this fault segment, although the east-west displacement extends nearly throughout the entire rupture zone. The motions on opposite sides of the fault are consistent with the sinistral-slip fault motion and the spatial distribution of the aftershocks. Using this information, we built a fault slip model comprising two fault segments and determined the corresponding segment surface traces (Figure 2). The spatial distribution of the aftershocks implies the eastern fault segment dips steeply (cross-section A-A′ in Figure 1d), whereas the western segment is likely less steep because of normal faulting (cross-section B-B′ in Figure 1e). Fixing the location of the surface traces, we performed many static inversions to search the optimal dip angles for the western and eastern fault segments (Text S1). The downdip width of each fault segment was set as 24 km, and the fault planes were then discretized into 2 km × 2 km subfaults.

We obtained a preferred two-segment source model by the joint inversion of the LOS displacements of three Sentinel-1 interferograms, the three-component broadband seismograms of 10 regional stations, and 38 teleseismic *P* waves. The unwrapped LOS displacements were subsampled using the quadtree method (Jónsson et al., 2002), and the Green's functions for the regional waveform and InSAR data were calculated using the frequency wavenumber integration code (Zhu & Rivera, 2002). From the near-field to regional range of the source area, the velocity structure model (Table S2) was considered horizontally layered (Chai et al., 2015). Based on the CRUST1.0 model (Laske et al., 2013), the Green's functions of teleseismic *P* waves were generated by Multitel3 developed by Qian et al. (2017), considering both direct and core-reflected waves. In accordance with the *W*-phase moment tensor, the slip rake of the subfaults was allowed within $-24 \pm 45°$. Our inversion exploited the linear multi-time-window method (Hartzell & Heaton, 1983; Olson & Apsel, 1982) to resolve the spatiotemporal source rupture process, with further details available in Zheng et al. (2018). Considering the trade-off between the rupture propagating velocity (the triggering speed of the first time window) and the rise time of time window, rupture velocities from 2.0 to 3.0 km/s (corresponding to 60–85% of the local *S* wave speed) with an interval of 0.2 km/s and rise times from 0.8 to 3.6 s with an interval of 0.4 s were tested (Figure S3). After a systematic grid search, a rupture velocity of 2.6 km/s was selected, allowing a maximum duration of 8.4 s within six half-overlapping triangle time windows. All data sets were initially normalized by the corresponding Frobenius norms (Chen et al., 2018), and the preferred weighting schemes for the InSAR, regional waveform, and teleseismic *P* wave data are 1.0, 0.4, and 0.2, respectively. A revised Laplacian smoothing (Zheng et al., 2020) was introduced to stabilize the inversion, and the smoothing factor chosen is consistent with the classic L-curve method (Figure S3).

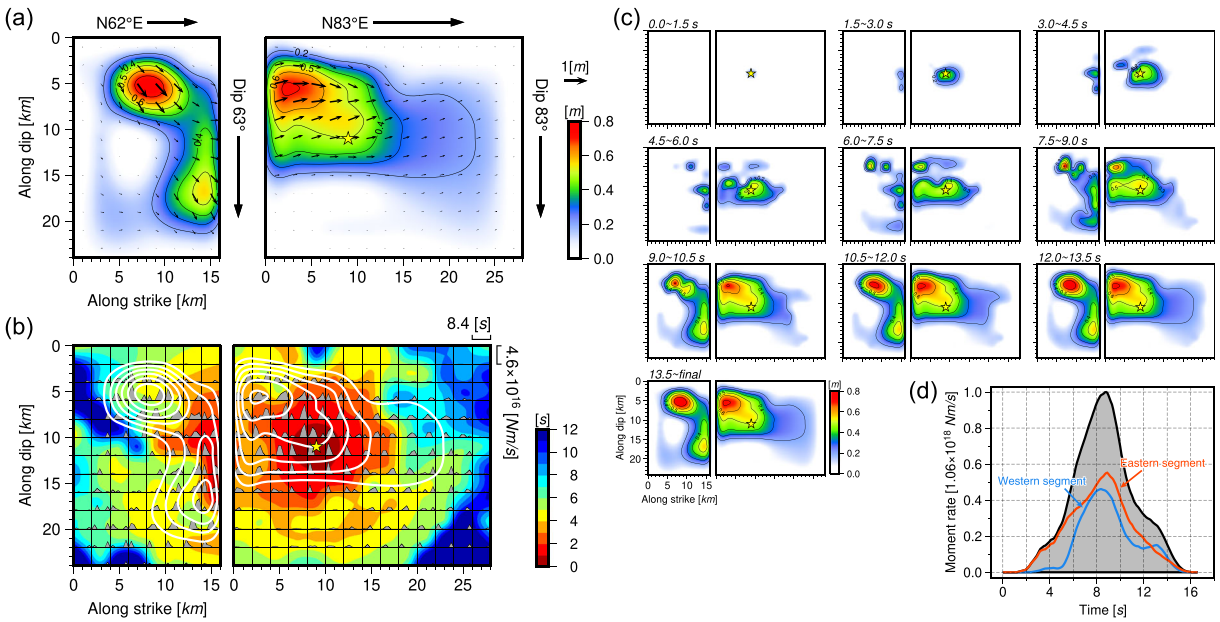

Figure 3. (a) Slip distribution according to our preferred two-segment fault model from the joint inversion. The slip contour interval is 0.1 m, and the yellow star is the rupture starting point. (b) Seismic moment releasing rate functions of the subfaults in the two-segment fault model, with the rupture front evolution with time as the background, and the slip contours shown by white lines. (c) Evolution of the cumulative fault slip of the two-segment fault model derived from the joint inversion. The contour interval is 0.1 m, and the yellow star indicates the rupture starting point. (d) Total seismic moment releasing rate functions of the two-segment fault model. The individual moment releasing rate functions of the western and eastern fault segments are plotted in blue and orange lines, respectively.

We also designed a simple single-fault model and a complex three-segment fault model to examine the suitability of these models for explaining the source complexity (Texts S2 and S3). As the simple single-fault model involves one fault segment, its source parameters were estimated by resolving the teleseismic *P* waves. The three-segment fault model is identical to our preferred model, except that it includes a third segment to accommodate dextral slips to the east. The same data, source parameter settings, and inversion method were utilized for the one-segment and three-segment fault models.

4. Results

Our best fitting model reveals that the fault dips steeply at 83° in the eastern segment and gently at 63° in the western segment. Further, the slip distribution of our preferred model shows different faulting patterns in the two fault segments (Figure 3a). Oblique fault slips are concentrated on the shallower part of the western segment, with a peak slip of approximately 0.8 m at about 4 km depth. Another asperity of minor slips of approximately 0.5 m occurs at depths between 13 and 18 km. A major sinistral-slip asperity is localized on the eastern segment, where the maximum slip attains 0.7 m. Few coseismic fault slips are obtained near the surface, suggesting that the event mostly manifested at depth. The source rupture is initiated on the eastern segment, and it involves a circular expansion, but the rupture front generally turns into a bilateral pattern with a rather uneven shape (Figures 3b and 3c). The western segment starts to rupture almost synchronously with the eastern segment, with a propagating delay of approximately 1 s. The rupture then migrates into the western segment from its eastern edge (Figure 3c). The moment releasing of the fault segments are comparable in time, and so, discriminating the contributions of individual segments from the single peak of the source time function is difficult, as depicted in Figure 3d. The total rupture duration is 16 s, reaching the maximum moment rate at approximately 9 s and releasing a scalar seismic moment of 7.8×10^{18} Nm (M_w 6.5). Furthermore, we synthesized the focal mechanism of this event from the cumulative moment tensor of the subfaults (Heimann et al., 2017), and it displays a nondouble-couple component of ~29% (Figure 1). This result is similar to the *W*-phase moment tensor of the USGS-NEIC and confirms the complexity of the source geometry and the faulting pattern.

The examined geodetic and seismic data are well resolved by our preferred model (Figures 2f–2j and S4). The variance reductions (VRs) for the InSAR LOS data, regional seismograms, and teleseismic *P* waves are 94%, 86%, and 66%, respectively. The deformation fringes in the ascending image exhibit a typical butterfly-shaped displacement pattern (Figure 2a), while complex deformation patterns are observed in the descending tracks (Figures 2b and 2c). The southwestern quadrants in all images show a strong negative LOS displacement, suggesting that the ground primarily moved away from the satellite and the area subsided. The subsided area implies the normal-faulting component existed on the western fault segment but was obscured in the focal mechanism revealed by the *W*-phase moment tensor, which is dominated by the strike-slip component. We also synthesized waveforms, including teleseismic *P* waves and regional seismograms, using our preferred source model but excluding the normal-faulting component on the western segment (Figure S6). Some of them are well resolved, whereas the participation of the normal slips on the western segment is still essential to fit all seismic waveforms. Normal fault slips were rarely observed in the Mina deflection before the 2020 event. Nevertheless, the joint inversion combining geodetic and seismic data provides better observation constraints and reveals the existence of the normal-faulting component for this earthquake.

5. Discussion

5.1. Implications for Regional Tectonics

Our source model shows that the two modeled fault segments in the northeastern edge of the right-stepping Mina deflection are previously unmapped. Existing studies indicate that slip transfer occurs in the Mina deflection (Nagorsen-Rinke et al., 2013; Oldow, 1992, 2003; Oldow et al., 1994; Wesnousky, 2005a), but there is no evidence for normal fault slip on the NE-striking sinistral faults (DeLano et al., 2019). The global positioning system velocities, earthquake focal mechanisms, and fault-slip inversions suggest that the western part of the Mina deflection is currently accommodated by extension-dominated transtension, and the eastern part is wrench-dominated (Hammond & Thatcher, 2004; Oldow, 2003). However, these studies were conducted primarily to the south of the main active part of the Mina deflection (Faulds et al., 2008). The northeastern Mina deflection, where the 2020 earthquake occurred, is historically characterized by low seismicity. Based on the joint inversion, the synthesized moment tensors of the two fault segments are shown in Figure 4b. If following the angular relationship between the incremental extensional axes and the dextral boundary faults (Fossen & Tikoff, 1993), with similar NW-trending extensional strain axes (*T* axis), the wrench-dominated transtension tectonics requires sinistral slip for both fault segments. However, the accommodation of slip transfer involving oblique slip in the west and sinistral slip in the east as revealed by the source mechanism of the 2020 event differs from the existing model of wrench-dominated transtension. This implies that the wrench-dominated transtension is not completely appropriate for the present-day deformation mechanism of the northeastern Mina deflection. The wrench or extension dominance of transtention depends on the ratio of the components of simple to pure shear contributing to the local strain (Fossen & Tikoff, 1993). During the transtensional deformation in a releasing stepover like the Mina deflection, the extensional pure shear accumulates faster compared with the wrench simple shear (De Paola et al., 2008; Tikoff & Greene, 1997; Tikoff & Teyssier, 1994). Moreover, the western fault segment is farther from the eastern dextral boundary fault, thereby facilitating the accumulation of the extensional pure shear. Consequently, with increasing finite strain, the wrench-dominated transtension localized in the western fault segment probably has a tendency to evolve into the extension-dominated transtension, and the initially horizontal compressional strain axis (*P* axis in Figure 4b) is becoming vertical (De Paola et al., 2008; Tikoff & Greene, 1997; Tikoff & Teyssier, 1994).

In addition, a general decrease in the organization and maturation seems plausible from south to north in the Walker Lane (Faulds et al., 2008). The irregularity and roughness of the source rupture demonstrate that the seismogenic fault for the 2020 Monte Cristo Range earthquake is immature and less developed than the southern boundary faults of the Mina deflection. During long-term tectonic deformation, the seismogenic fault could originate from sinistral Riedel shears (Petit, 1987) that are conjugate to the NW-striking dextral faults. However, influenced by the local strain field, the western fault segment turns into an oblique-slip fault, whereas the eastern fault segment retains the strike-slip faulting pattern. A major portion of the dextral slip rotating clockwise might be responsible for the orientation changes of fault segments from east to west.

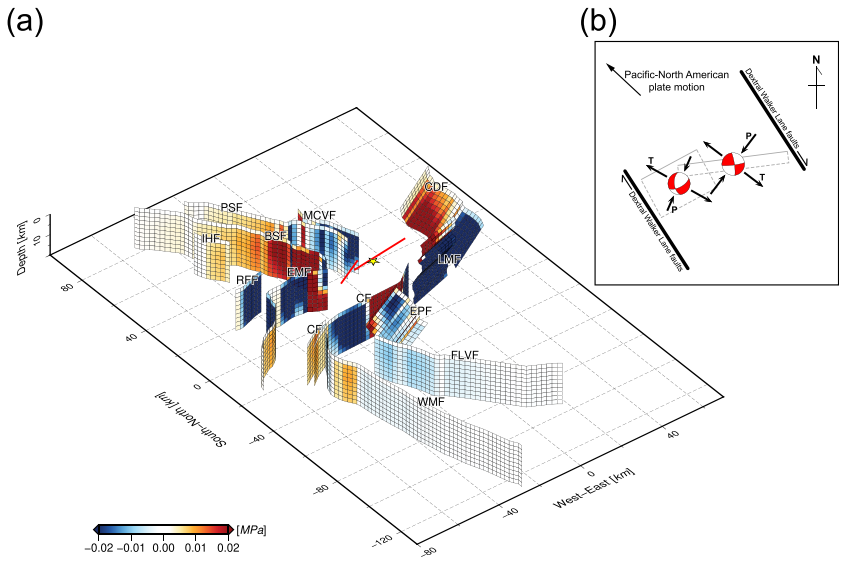

Figure 4. (a) Distribution of the static CFS changes in the surrounding active faults induced by the 2020 Monte Cristo Range earthquake. The Skempton's coefficient and the friction coefficient were separately assumed as 0.5 and 0.8, equivalent to an effective friction coefficient of 0.4. The fault abbreviations are identical to those in Figure 1a. The red lines represent the top traces of the two-segment fault model, with the yellow star as the epicenter. (b) Conceptual illustration of the present-day deformation mechanism in the northeastern Mina deflection stepover as revealed by the 2020 Monte Cristo Range earthquake. The focal mechanisms of the two fault segments were synthesized based on the joint inversion result. The paired arrows with opposite directions separately represent the extensional strain axis (*T* axis) or the compressional strain axis (*P* axis). Because of the obliquity between the plate motion and the orientation of dextral faults, the deformation in the Mina deflection is generally interpreted as transtension. Within the dextral boundary shear, the oblique slips on the western fault segment indicate the localized accommodation of slip transfer probably has a tendency to evolve into the extension-dominated transtension, and the initially horizontal compressional strain axis (*P* axis) is becoming vertical.

5.2. Regional Seismic Hazard Evaluation

The seismic stress triggering theory indicates that regional stress accumulated by tectonic motion is released when earthquakes occur. The released stress is redistributed and influences the subsequent seismicity triggering other earthquakes (King et al., 1994; Stein et al., 1994). Based on the two-segment fault model, the static Coulomb failure stress (CFS) changes induced by the 2020 Monte Cristo Range earthquake in the surrounding active faults were calculated using different friction coefficients (Text S5). The geometry for the receiver faults was adopted from Petersen et al. (2014). The nearly NS-trending Benton Springs and Petrified Springs faults are two major dextral faults in the central Walker Lane. As shown in Figure 4a, the CFS on the southern segment of the Benton Springs fault near the western segment of the source fault is increased by 0.09 MPa, while the Monte Cristo Valley fault and the adjacent southern segment of the Petrified Springs fault near the eastern segment are in a stress shadow zone. The orientation and faulting pattern difference between the two modeled fault segments are probably responsible for the variable CFS changes induced in these dextral receiver faults. The Excelsior Mountains and Coaldale faults are sinistral faults defining the Mina deflection. The positive CFS change on the eastern segment of the Excelsior Mountains fault expands and increases with the friction coefficient, ranging from 0.06 to 0.09 MPa. The remaining part of the Excelsior Mountains fault alongside the Rattlesnake Flat fault and the western segment of the Coaldale fault reflects stress unloading. The calculated CFS change on the eastern segment of the Coaldale fault is positively associated with the friction coefficient, ranging from 0.10 to 0.16 MPa, and far exceeds the earthquake triggering threshold 0.01 MPa (Hardebeck et al., 1998), suggesting the seismic hazard for the Coaldale and Benton Springs faults may be potentially increased.

5.3. Other Possible Fault-Slip Models

Although our preferred fault model comprises two fault segments, examining a simple single-fault model (Figures S8–S10) and a three-segment fault model (Figures S11–S15) provides good data fitting and

explains the complexity of the event using the same inversion strategy. The teleseismic *P* waves are well resolved by the single-fault model, with a corresponding VR of 69%. The slip distribution of the single-fault model is displayed in Figure S8, highlighting a rather complex slip pattern for a moderate earthquake of M_w 6.5, for which an oblique-slip asperity occurs in the western part of the fault plane, and the eastern part involves almost purely strike-slip faulting. The oblique and sinistral slip separation is consistent with the complex faulting pattern inferred from the east-west and vertical displacement fields, but the single-fault model inadequately explains the fault geometry variations in the interferograms. Conversely, the joint inversion of the three-segment fault model yields VRs for the InSAR LOS data, regional seismograms, and teleseismic *P* waves of 95%, 87%, and 68%, respectively, which is comparable to the results of our preferred two-segment fault model. The inversion results for the three-segment fault model suggest that minor slips occur on the third fault segment with the peak slip not exceeding 0.3 m, which is nearly negligible, whereas the slip distribution of the other two segments resembles that of the preferred two-segment fault model (Figure S12). Moreover, the CFS changes calculated using the slips on the western and middle segments of the three-segment fault model cannot support triggering the rupture of the third fault segment (Figure S16). Hence, the two-segment fault model adequately fits the observed ground deformation fields, the broadband seismic data, and the source complexity of the 2020 Monte Cristo Range earthquake.

6. Conclusions

We investigated the source rupture process of the 2020 Monte Cristo Range earthquake through the joint inversion of the InSAR and broadband seismic data. The source fault comprises two main segments with different orientations, and the coseismic slip distribution demonstrates that these segments are dominated by distinct faulting patterns. The eastern segment exhibits characteristics of a sinistral fault, whereas the western segment contains the sinistral and normal-faulting components. The present-day deformation mechanism of the northeastern Mina deflection revealed by the 2020 Monte Cristo Range earthquake partially differs from existing models. The distinct faulting patterns of the two fault segments indicate that the slip transfer across the Mina deflection is incompletely accommodated by the wrench-dominated transtension. The deformation mechanism of the area hosting the western fault segment was probably influenced by the local stress field, tending to transform into the extension-dominated transtension. The complexity and irregularity of the source rupture imply that the unmapped seismogenic fault is immature. Moreover, due to the CFS increase caused by the 2020 event, the potential seismic hazard associated with the Benton Springs and the Coaldale faults deserves further attention.

Data Availability Statement

Teleseismic and regional seismic waveforms were recorded by the International Federation of Digital Seismograph Networks (FDSN), accessed through IRIS DMC. All waveform data were processed by ObsPy (Krischer et al., 2015). This work also used Copernicus data from the Sentinel-1 satellite constellation provided by the European Space Agency (https://scihub.copernicus.eu). The InSAR data processing made use of the GAMMA software (supporting the entire processing chain from synthetic aperture radar raw data to end products such as displacement maps, digital elevation models, etc.) and MATLAB. All processed InSAR data are available from the authors upon request. The information of aftershocks was provided by USGS-NEIC (https://earthquake.usgs.gov/earthquakes/search/). The Generic Mapping Tools (GMT) developed by Wessel and Smith (1998) was used to plot the figures.

Acknowledgments

We thank the Editor Lucy Flesch, Shaoyang Li, and an anonymous reviewer for their helpful reviews. This work is supported by the National Natural Science Foundation of China (grants 41804015, U1901602, and 41790465).

References

Bennett, R. A., Wernicke, B. P., Niemi, N. A., Friedrich, A. M., & Davis, J. L. (2003). Contemporary strain rates in the northern Basin and Range province from GPS data. *Tectonics*, *22*(2), 1008. https://doi.org/10.1029/2001TC001355

Chai, C. P., Ammon, C. J., Maceira, M., & Herrmann, R. B. (2015). Inverting interpolated receiver functions with surface wave dispersion and gravity: Application to the western US and adjacent Canada and Mexico. *Geophysical Research Letters*, *42*, 4359–4366. https://doi.org/10.1002/2015GL063733

Chen, C. W., & Zebker, H. A. (2001). Two-dimensional phase unwrapping with use of statistical models for cost functions in nonlinear optimization. *Journal of the Optical Society of America A*, *18*(2), 338–351. https://doi.org/10.1364/josaa.18.000338

Chen, K. J., Xu, W. B., Mai, P. M., Gao, H., Zhang, L., & Ding, X. L. (2018). The 2017 Mw 7.3 Sarpol Zahab earthquake, Iran: A compact blind shallow-dipping thrust event in the mountain front fault basement. *Tectonophysics*, *747–748*, 108–114. https://doi.org/10.1016/j.tecto.2018.09.015

De Paola, N., Holdsworth, R. E., & Colleitini, C. (2008). The internal structure of dilational stepovers in regional transtension zones. *International Geology Review*, *50*(3), 291–304. https://doi.org/10.2747/0020-6814.50.3.291

DeLano, K., Lee, J., Roper, R., & Calvert, A. (2019). Dextral, normal, and sinistral faulting across the eastern California shear zone-Mina deflection transition, California-Nevada, USA. *Geosphere*, *15*(4), 1206–1239. https://doi.org/10.1130/Ges01636.1

DeMets, C., & Dixon, T. H. (1999). New kinematic models for Pacific-North America motion from 3 Ma to present, I: Evidence for steady motion and biases in the NUVEL-1A model. *Geophysical Research Letters*, *26*(13), 1921–1924. https://doi.org/10.1029/1999GL900405

Dixon, T. H., Miller, M., Farina, F., Wang, H. Z., & Johnson, D. (2000). Present-day motion of the Sierra Nevada block and some tectonic implications for the Basin and Range province, North American Cordillera. *Tectonics*, *19*(1), 1–24. https://doi.org/10.1029/1998TC001088

Dixon, T. H., Robaudo, S., Lee, J., & Reheis, M. C. (1995). Constraints on present-day Basin and Range deformation from space geodesy. *Tectonics*, *14*(4), 755–772. https://doi.org/10.1029/95TC00931

Dokka, R. K., & Travis, C. J. (1990). Late Cenozoic strike-slip faulting in the Mojave Desert, California. *Tectonics*, *9*(2), 311–340. https://doi.org/10.1029/TC009i002p00311

Farr, T. G., Rosen, P. A., Caro, E., Crippen, R., Duren, R., Hensley, S., et al. (2007). The shuttle radar topography mission. *Reviews of Geophysics*, *45*, RG2004. https://doi.org/10.1029/2005RG000183

Faulds, J. E., Henry, C. D., & Hinz, N. H. (2005). Kinematics of the northern Walker Lane: An incipient transform fault along the Pacific-North American plate boundary. *Geology*, *33*(6), 505–508. https://doi.org/10.1130/G21274.1

Faulds, J. E., Henry, C. D., Spencer, J. E., & Titley, S. R. (2008). Tectonic influences on the spatial and temporal evolution of the Walker Lane: An incipient transform fault along the evolving Pacific–North American plate boundary. *Ores and orogenesis: Circum-Pacific tectonics, geologic evolution, and ore deposits: Arizona Geological Society Digest*, *22*, 437–470.

Fossen, H., & Tikoff, B. (1993). The deformation matrix for simultaneous simple shearing, pure shearing and volume change, and its application to transpression transtension tectonics. *Journal of Structural Geology*, *15*(3–5), 413–422. https://doi.org/10.1016/0191-8141(93)90137-Y

Hammond, W. C., & Thatcher, W. (2004). Contemporary tectonic deformation of the Basin and Range province, western United States: 10 years of observation with the Global Positioning System. *Journal of Geophysical Research*, *109*, B08403. https://doi.org/10.1029/2003JB002746

Hardebeck, J. L., Nazareth, J. J., & Hauksson, E. (1998). The static stress change triggering model: Constraints from two southern California aftershock sequences. *Journal of Geophysical Research*, *103*(B10), 24,427–24,437. https://doi.org/10.1029/98JB00573

Hartzell, S. H., & Heaton, T. H. (1983). Inversion of strong ground motion and teleseismic waveform data for the fault rupture history of the 1979 Imperial Valley, California, earthquake. *Bulletin of the Seismological Society of America*, *73*(6), 1553–1583.

Heimann, S., Kriegerowski, M., Isken, M., Cesca, S., Daout, S., Grigoli, F., et al. (2017). Pyrocko-An open-source seismology toolbox and library. *GFZ Data Services*. https://doi.org/10.5880/GFZ.2.1.2017.001

Hodgkinson, K. M., Stein, R. S., & King, G. C. P. (1996). The 1954 rainbow Mountain-Fairview Peak-Dixie Valley earthquakes: A triggered normal faulting sequence. *Journal of Geophysical Research*, *101*(B11), 25,459–25,471. https://doi.org/10.1029/96JB01302

Jónsson, S., Zebker, H., Segall, P., & Amelung, F. (2002). Fault slip distribution of the 1999 Mw 7.1 Hector Mine, California, earthquake, estimated from satellite radar and GPS measurements. *Bulletin of the Seismological Society of America*, *92*(4), 1377–1389. https://doi.org/10.1785/0120000922

Kikuchi, M., & Kanamori, H. (1982). Inversion of complex body waves. *Bulletin of the Seismological Society of America*, *72*(2), 491–506.

King, G. C. P., Stein, R. S., & Lin, J. (1994). Static stress changes and the triggering of earthquakes. *Bulletin of the Seismological Society of America*, *84*(3), 935–953.

Krischer, L., Megies, T., Barsch, R., Beyreuther, M., Lecocq, T., Caudron, C., & Wassermann, J. (2015). ObsPy: A bridge for seismology into the scientific Python ecosystem. *Computational Science & Discovery*, *8*(1), 014003. https://doi.org/10.1088/1749-4699/8/1/014003

Laske, G., Masters, G., Ma, Z., & Pasyanos, M. (2013). Update on CRUST1.0—A 1-degree global model of Earth's crust. EGU General Assembly Conference Abstracts, 15, EGU2013-2658.

Lee, J., Garwood, J., Stockli, D. F., & Gosse, J. (2009). Quaternary faulting in Queen Valley, California-Nevada: Implications for kinematics of fault-slip transfer in the eastern California shear zone-Walker Lane belt. *Geological Society of America Bulletin*, *121*(3–4), 599–614. https://doi.org/10.1130/B26352.1

Li, Z. W., Ding, X., Huang, C., Zhu, J. J., & Chen, Y. L. (2008). Improved filtering parameter determination for the Goldstein radar interferogram filter. *ISPRS Journal of Photogrammetry and Remote Sensing*, *63*(6), 621–634. https://doi.org/10.1016/j.isprsjprs.2008.03.001

Massonnet, D., Rossi, M., Carmona, C., Adragna, F., Peltzer, G., Feigl, K., & Rabaute, T. (1993). The displacement field of the Landers earthquake mapped by radar interferometry. *Nature*, *364*(6433), 138–142. https://doi.org/10.1038/364138a0

Nagorsen-Rinke, S., Lee, J., & Calvert, A. (2013). Pliocene sinistral slip across the Adobe Hills, eastern California-western Nevada: Kinematics of fault slip transfer across the Mina deflection. *Geosphere*, *9*(1), 37–53. https://doi.org/10.1130/Ges00825.1

Oldow, J. S. (1992). Late Cenozoic displacement partitioning in the northwestern Great Basin. In S. D. Graig (Ed.), *Structure, Tectonics, and Mineralization of the Walker Lane* (pp. 17-52). Reno, Nevada: Geological Society of Nevada Walker Lane Symposium Proceedings Volume.

Oldow, J. S. (2003). Active transtensional boundary zone between the western Great Basin and Sierra Nevada block, western US cordillera. *Geology*, *31*(12), 1033–1036. https://doi.org/10.1130/G19838.1

Oldow, J. S., Kohler, G., & Donelick, R. A. (1994). Late Cenozoic extensional transfer in the Walker Lane strike-slip belt, Nevada. *Geology*, *22*(7), 637–640. https://doi.org/10.1130/0091-7613(1994)022<0637:Lcetit>2.3.Co;2

Olson, A. H., & Apsel, R. J. (1982). Finite faults and inverse-theory with applications to the 1979 Imperial Valley earthquake. *Bulletin of the Seismological Society of America*, *72*(6), 1969–2001.

Petersen, M. D., Frankel, A. D., Harmsen, S. C., Mueller, C. S., Haller, K. M., Wheeler, R. L., et al. (2014). Documentation for the 2014 update of the United States national seismic hazard maps. *U.S. Geological Survey Open-File Report*. 2014-1091. https://doi.org/10.3133/ofr20141091

Petit, J. P. (1987). Criteria for the sense of movement on fault surfaces in brittle rocks. *Journal of Structural Geology*, *9*(5–6), 597–608. https://doi.org/10.1016/0191-8141(87)90145-3

Qian, Y. Y., Ni, S. D., Wei, S. J., Almeida, R., & Zhang, H. (2017). The effects of core-reflected waves on finite fault inversions with teleseismic body wave data. *Geophysical Journal International*, *211*(2), 936–951. https://doi.org/10.1093/gji/ggx338

Rogers, A. M., Harmsen, S. C., Corbett, E. J., Priestley, K., & dePolo, D. (1991). The seismicity of Nevada and some adjacent parts of the Great Basin. *Neotectonics of North America*, *1*, 153–184.

Stein, R. S., King, G. C. P., & Lin, J. (1994). Stress triggering of the 1994 M = 6.7 Northridge, California, earthquake by its predecessors. *Science*, *265*(5177), 1432–1435. https://doi.org/10.1126/science.265.5177.1432

Tikoff, B., & Greene, D. (1997). Stretching lineations in transpressional shear zones: An example from the Sierra Nevada Batholith, California. *Journal of Structural Geology*, *19*(1), 29–39. https://doi.org/10.1016/S0191-8141(96)00056-9

Tikoff, B., & Teyssier, C. (1994). Strain modeling of displacement-field partitioning in transpressional orogens. *Journal of Structural Geology*, *16*(11), 1575–1588. https://doi.org/10.1016/0191-8141(94)90034-5

Tincher, C. R., Stockli, D. F., Oldow, J. S., & Cashman, P. H. (2009). Cenozoic volcanism and tectonics in the Queen Valley area, Esmeralda County, western Nevada. *Late Cenozoic structure and evolution of the Great Basin-Sierra Nevada transition: Geological Society of America Special Paper*, *447*, 255–274.

Wald, D. J., Heaton, T. H., & Hudnut, K. W. (1996). The slip history of the 1994 Northridge, California, earthquake determined from strong-motion, teleseismic, GPS, and leveling data. *Bulletin of the Seismological Society of America*, *86*(1), S49–S70.

Wesnousky, S. G. (2005a). Active faulting in the Walker Lane. *Tectonics*, *24*, TC3009. https://doi.org/10.1029/2004tc001645

Wesnousky, S. G. (2005b). The San Andreas and Walker Lane fault systems, western North America: Transpression, transtension, cumulative slip and the structural evolution of a major transform plate boundary. *Journal of Structural Geology*, *27*(8), 1505–1512. https://doi.org/10.1016/j.jsg.2005.01.015

Wessel, P., & Smith, W. H. F. (1998). New, improved version of Generic Mapping Tools released. *Eos, Transactions American Geophysical Union*, *79*(47), 579–579. https://doi.org/10.1029/98EO00426

Xu, W., Jónsson, S., Ruch, J., & Aoki, Y. (2016). The 2015 Wolf volcano (Galapagos) eruption studied using Sentinel-1 and ALOS-2 data. *Geophysical Research Letters*, *43*, 9573–9580. https://doi.org/10.1002/2016GL069820

Zheng, A., Wang, M., Yu, X., & Zhang, W. (2018). Source rupture process of the 2016 Kaikoura, New Zealand earthquake estimated from the kinematic waveform inversion of strong-motion data. *Geophysical Journal International*, *212*(3), 1736–1746. https://doi.org/10.1093/gji/ggx505

Zheng, A., Yu, X., Xu, W., Chen, X., & Zhang, W. (2020). A hybrid source mechanism of the 2017 Mw 6.5 Jiuzhaigou earthquake revealed by the joint inversion of strong-motion, teleseismic and InSAR data. *Tectonophysics*, *789*, 228538. https://doi.org/10.1016/j.tecto.2020.228538

Zhu, L., & Rivera, L. A. (2002). A note on the dynamic and static displacements from a point source in multilayered media. *Geophysical Journal International*, *148*(3), 619–627. https://doi.org/10.1046/j.1365-246X.2002.01610.x

Reference From the Supporting Information

Wang, R., Lorenzo-Martín, F., & Roth, F. (2006). PSGRN/PSCMP—A new code for calculating co- and post-seismic deformation, geoid and gravity changes based on the viscoelastic-gravitational dislocation theory. *Computers & Geosciences*, *32*(4), 527–541. https://doi.org/10.1016/j.cageo.2005.08.006